

RESEARCH ARTICLE

10.1002/2016JE005166

Key Points:

- First detailed mapping and documentation of magnetic anomalies in the lunar Imbrium basin
- Same for the Schrödinger basin
- Anomalies in these basins are most easily understood if the former core dynamo existed but was weaker during the Imbrian period

Supporting Information:

- Supporting Information S1

Correspondence to:

L. L. Hood,
lon@lpl.arizona.edu

Citation:

Hood, L. L., and P. D. Spudis (2016), Magnetic anomalies in the Imbrium and Schrödinger impact basins: Orbital evidence for persistence of the lunar core dynamo into the Imbrian epoch, *J. Geophys. Res. Planets*, 121, doi:10.1002/2016JE005166.

Received 7 SEP 2016

Accepted 28 OCT 2016

Accepted article online 7 NOV 2016

Magnetic anomalies in the Imbrium and Schrödinger impact basins: Orbital evidence for persistence of the lunar core dynamo into the Imbrian epoch

L. L. Hood¹ and P. D. Spudis²

¹Lunar and Planetary Laboratory, University of Arizona, Tucson, Arizona, USA, ²Lunar and Planetary Institute, Houston, Texas, USA

Abstract Approximate maps of the lunar crustal magnetic field at low altitudes in the vicinities of the three Imbrian-aged impact basins, Orientale, Schrödinger, and Imbrium, have been constructed using Lunar Prospector and Kaguya orbital magnetometer data. Detectable anomalies are confirmed to be present well within the rims of Imbrium and Schrödinger. Anomalies in Schrödinger are asymmetrically distributed about the basin center, while a single isolated anomaly is most clearly detected within Imbrium northwest of Timocharis crater. The subsurface within these basins was heated to high temperatures at the time of impact and required long time periods (up to 1 Myr) to cool below the Curie temperature for metallic iron remanence carriers (1043 K). Therefore, consistent with laboratory analyses of returned samples, a steady, long-lived magnetizing field, i.e., a former core dynamo, is inferred to have existed when these basins formed. The asymmetrical distribution within Schrödinger suggests partial demagnetization by later volcanic activity when the dynamo field was much weaker or nonexistent. However, it remains true that anomalies within Imbrian-aged basins are much weaker than those within most Nectarian-aged basins. The virtual absence of anomalies within Orientale where impact melt rocks (the Maunder Formation) are exposed at the surface is difficult to explain unless the dynamo field was much weaker during the Imbrian period.

1. Introduction

Laboratory analyses of returned samples indicate that a lunar core dynamo with surface fields of tens of μT existed at ~ 4.2 Gyr ago [Garrick-Bethell *et al.*, 2009] and persisted at least until ~ 3.7 Gyr [Shea *et al.*, 2012; Cournède *et al.*, 2012; Suavet *et al.*, 2013; Tikoo *et al.*, 2014; Weiss and Tikoo, 2014]. A recent analysis of a lunar regolith breccia indicates a much weaker or nonexistent surface field ($< 0.1 \mu\text{T}$) at ~ 1 Gyr ago [Wang and Weiss, 2016]. For comparison, the lunar Imbrian period commenced at the time of the Imbrium impact at ~ 3.9 Gyr ago [e.g., Merle *et al.*, 2014] and continued until the time of the Eratosthenes crater-forming event at about 3.1 Gyr ago [Wilhelms, 1987].

Analyses of orbital data to confirm these laboratory constraints on lunar internal evolution are generally difficult because of evidence that impact processes (specifically impact ejecta deposition and shock magnetization and demagnetization) have contributed to the production and destruction of magnetic anomaly sources on the Moon [e.g., Strangway *et al.*, 1973; Hood *et al.*, 2001, 2013; Halekas *et al.*, 2001, 2002; Gattacceca *et al.*, 2010]. However, there is one class of lunar magnetic anomalies that is generally agreed to provide useful indicators of the existence or absence of a core dynamo at the times of their formation, i.e., magnetic anomalies within the rims of impact basins or large craters [Halekas *et al.*, 2003; Wieczorek and Weiss, 2010; Hood, 2011]. This is because the source materials of such anomalies, which probably lie beneath the visible mare basalt surfaces, must have formed via slow cooling (thermoremanent magnetization) in the presence of a steady, long-lived magnetizing field. The latter argument is suggested by the results of numerical impact simulations [e.g., Ivanov, 2005], which show that the subsurface within large crater rims was heated to high temperatures and required long periods (up to 1 Myr) to cool through the Curie blocking spectrum. Formation of these anomaly sources therefore required a steady, long-lived magnetizing field, i.e., a core dynamo field. Alternate field sources, e.g., an early strong solar wind field or a field amplified immediately after the impact, would either no longer be present or would change its orientation continuously leading to no coherent magnetization over a 1 Myr period.

Previous work has shown the existence of relatively strong central magnetic anomalies in a number of impact basins that formed in the Nectarian period [Halekas *et al.*, 2003; Hood, 2011]. These results are consistent with the laboratory data because estimates for the time of the Nectaris impact at the beginning of the Nectarian period range from ~ 3.9 Gyr [e.g., Ryder, 2002] up to ~ 4.2 Gyr ago [Fischer-Gödde and Becker, 2011, 2012]. Previous work has also shown the existence of weaker central anomalies in several pre-Nectarian basins [Hood *et al.*, 2014], which indicates that the onset of dynamo generation may have been prior to 4.2 Gyr. However, only very weak anomalies have previously been reported in impact basins that are as young or younger than ~ 3.9 Gyr (i.e., Imbrium, Schrödinger, and Orientale).

In this paper, more detailed mapping is reported of Kaguya (KG) and Lunar Prospector (LP) magnetometer data in the vicinities of the three Imbrian-aged basins. In section 2, the selection and preparation of the best available measurements over these basins are described. In section 3, the mapping methodology is described, and maps are presented and discussed. The existence of detectable anomalies within the basin rims is evaluated on the basis of examinations of individual orbit passes in section 2, while the distribution of any anomalies is evaluated in section 3. Discussion and conclusions are given in section 4.

2. Data Selection and Preparation

As noted in section 1, only three Imbrian-aged impact basins (defined as impact structures whose main rims are at least 300 km in diameter) exist. The largest of these is Imbrium (diameter ~ 1160 km; centered at $\sim 35^\circ\text{N}$, 343°E). The second largest and (probably) youngest basin is Orientale (diameter ~ 930 km; centered at $\sim 19^\circ\text{S}$, 265°E). The smallest and (probably) second youngest is Schrödinger (diameter ~ 316 km; centered at 75°S , 133°E).

Two complementary low-altitude orbital magnetometer data sets and one electron reflectometer data set are presently available for investigating the existence of crustal magnetic anomalies within these basin rims. These are those obtained by the Lunar Prospector (LP) magnetometer and electron reflectometer (ER) in 1998–1999 [Lin *et al.*, 1998; Hood *et al.*, 2001; Halekas *et al.*, 2001] and the Kaguya (KG) magnetometer in 2008–2009 [Tsunakawa *et al.*, 2010, 2015]. The LP magnetometer data set provides nearly global measurements at low altitudes but was obtained under solar maximum conditions when external (solar wind and magnetospheric) magnetic field variability was relatively large. The indirect ER measurements are therefore a valuable supplement to the LP magnetometer data. The KG data set was obtained under nearly ideal solar minimum conditions but provides low-altitude measurements mainly in the southern hemisphere and at very low northern latitudes. Thus, the LP data set usually provides the best available direct measurements at middle to high northern latitudes, while the KG data set provides highest quality measurements in the southern hemisphere. Both the LP and KG magnetometer data are freely available for download as described in the acknowledgments.

Previous mapping of magnetic anomalies near and within Imbrium has yielded some consistent evidence for the existence of weak magnetic anomalies. Maps of the lunar nearside constructed using LP ER data show weak anomalies within the rim of Imbrium [Halekas *et al.*, 2001, Plate 1; Halekas *et al.*, 2003, Figures 1 and 5; Mitchell *et al.*, 2008, Figures 4 and 5; Halekas *et al.*, 2010, Figure 5]. More recent global mapping of LP and KG magnetometer data also show weak anomalies within the Imbrium rim [Purucker and Nicholas, 2010, Figure 6; Tsunakawa *et al.*, 2015, Figures 2 and 4]. While the locations and relative amplitudes of these anomalies are often inconsistent from one map to another, some consistencies can be found. For example, an early spherical harmonic map [Purucker *et al.*, 2008] showed an anomaly near 343°E , 25°N that could be consistent with an anomaly near 344°E , 28°N on an ER map of Halekas *et al.* [2010]. But a detailed and documented map of the interior of Imbrium has not really been produced. Similarly, some weak anomalies near and within the Schrödinger and Orientale basins can be found on previous maps although the locations and amplitudes vary considerably from one map to another [see, e.g., Purucker *et al.*, 2008].

In order to evaluate further whether anomalies are detectable within the Imbrium, Schrödinger, and Orientale impact basins, all low-altitude magnetometer measurements obtained during the LP and KG missions were reexamined for coverage near and within these basins. In the case of Imbrium, a series of 29 LP orbits was selected from 14 to 18 April 1999 when the spacecraft altitude was very low (as low as 13 km) over this region. These orbits were for a period when the Moon was in the solar wind, but the spacecraft was centered in the lunar wake so that external field variations were reduced. Figure 1 shows a stack plot of the radial magnetic field component along 20 of these orbits after (a) editing to eliminate segments when external field variability

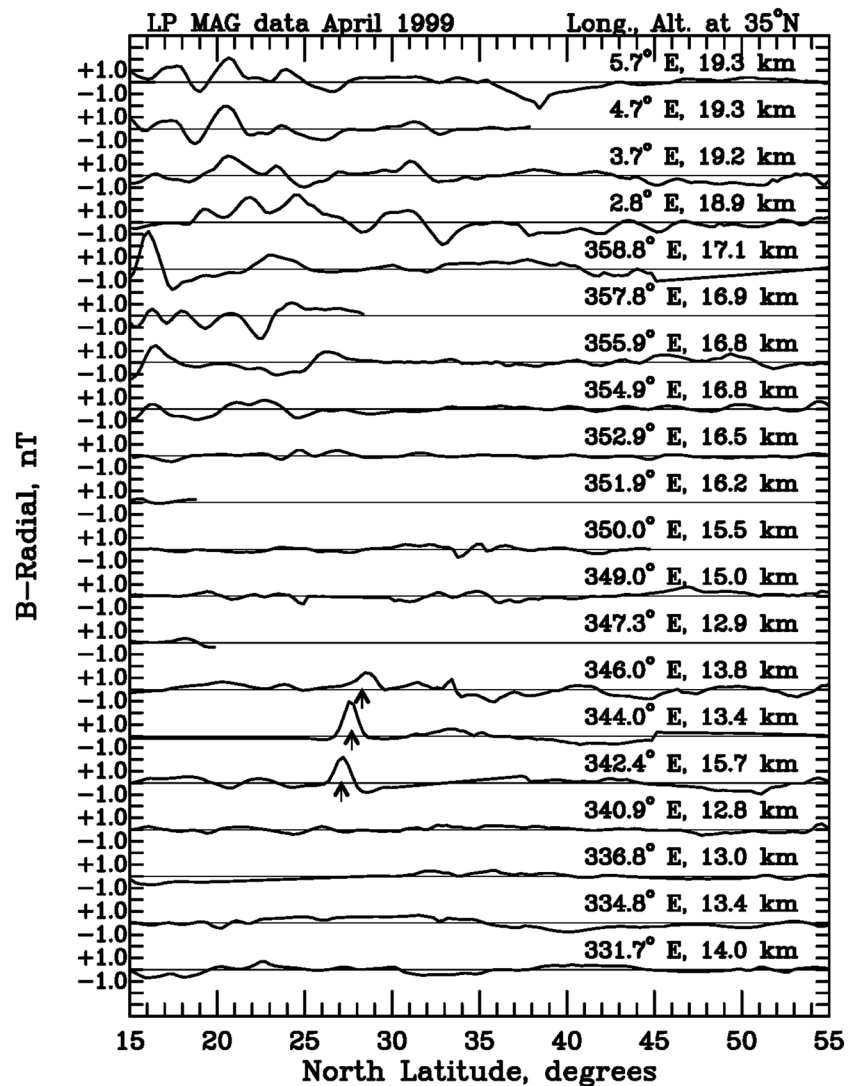


Figure 1. Radial magnetic field component along a series of Lunar Prospector orbit passes in April 1999 over the Imbrium basin after editing to remove passes containing significant external field contamination. All orbit segments were quadratically detrended to reduce long-wavelength, noncrustal variations. Arrows identify a repeating anomaly located well within the basin rim. Longitude and altitude at 35°N are indicated at right.

was unusually large and (b) quadratic detrending of the residual time series to minimize long-wavelength external field contributions. Specifically, adjacent orbit segments were first differenced to minimize the crustal field contribution and then segments whose radial component residuals had RMS deviations greater than 1.5 nT were eliminated. Quadratic detrending of remaining segments with lengths of 50° of latitude eliminates wavelengths longer than about 25° (750 km). Figures S1–S4 in the supporting information online illustrate the editing and detrending steps that were taken. Figures S5 and S6 show the final east and north components in the same format as Figure 1. As can be seen by comparing Figure 1 with Figures S5 and S6, the radial field component is less contaminated by external field variations. This is mainly because induced currents in the lunar upper mantle tend to suppress external field variations that are normal to the surface. The radial field component is therefore chosen as the primary mapping input.

As seen in Figure 1, although some external field contamination remains in most orbits, a number of anomalies are identifiable that repeat on successive orbits and are therefore confirmed to be of lunar origin. Many of the stronger ones (e.g., those near 5°E, 20°N) lie near or just outside the basin rim. However, one relatively strong and isolated anomaly with an amplitude of several nT is verified to be present well within the basin rim northwest of the crater Timocharis near 344°E, 28°N (indicated by vertical arrows). The existence of this anomaly

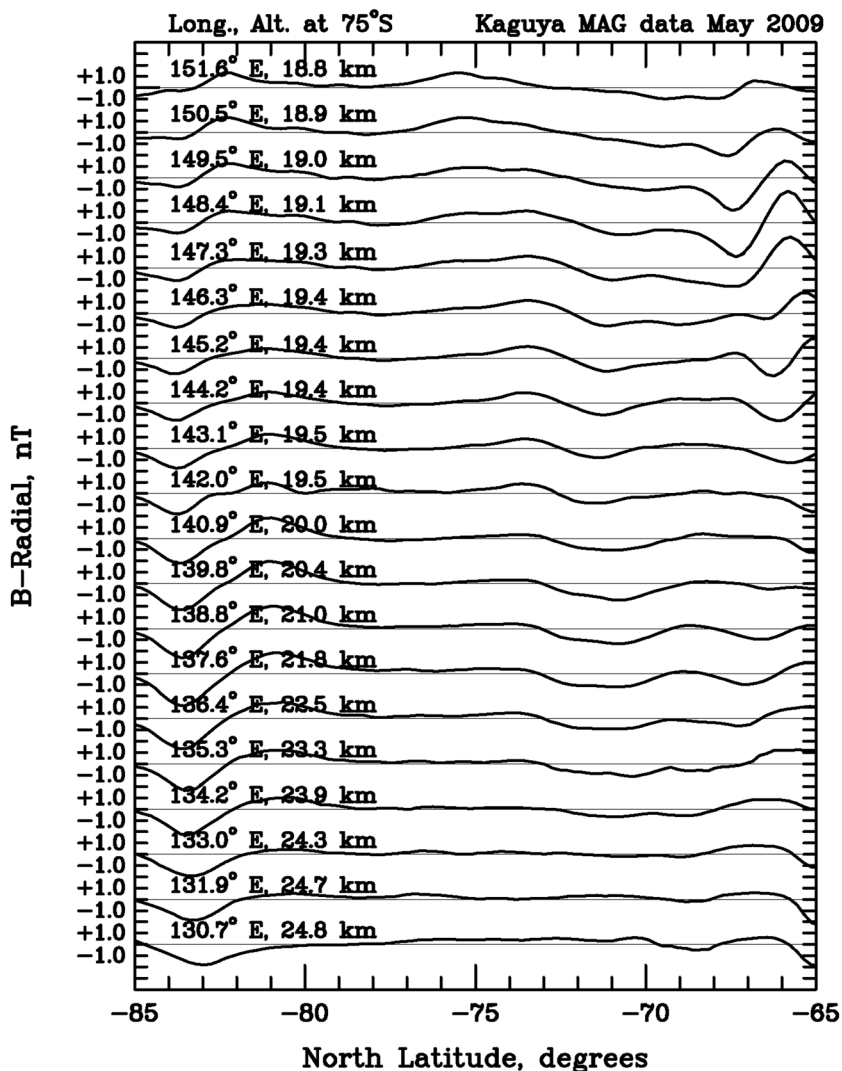


Figure 2. As in Figure 1 but for a series of Kaguya orbit passes from May 2009 over the Schrödinger impact basin in the south polar region. Longitude and altitude at 75°S are indicated at left.

has not been specifically reported previously to the authors' knowledge, although at least one previous ER map shows a surface field enhancement near this location [Halekas *et al.*, 2010, Figure 5]. It should be emphasized that weaker anomalies with amplitudes less than 1 nT may be undetectable elsewhere in Imbrium due to remaining external field contamination. However, it is clear that there is no other anomaly within the basin rim that is as strong as that detected on the two passes at longitudes of 342.4°E and 344.0°E.

In the case of Schrödinger, 57 low-altitude passes of the KG spacecraft obtained during 8–12 May 2009 over a region from 100°E to 160°E and from 65°S to 85°S were selected. The altitude of observation varied from ~19 km on the southeastern side to ~26 km on the western side of this region. These particular orbits occurred during a period when the Moon was in a lobe of the geomagnetic tail and so were relatively free of external field variations. Figure 2 plots the radial field component for a subset of these orbits for a latitude range bracketing the basin center at 75°S. For comparison, Figures S7 and S8 show the east and north field components. Much less external field contamination is present for all three components than was the case for the Imbrium data shown in Figures 1, S5, and S6. The same editing and detrending operations were applied as described above for the Imbrium passes but much less editing was required; almost all orbit passes were retained. Repeating anomalies are detectable on most passes, including areas that are well within the basin rim, which has boundaries at 115°E and 150°E.

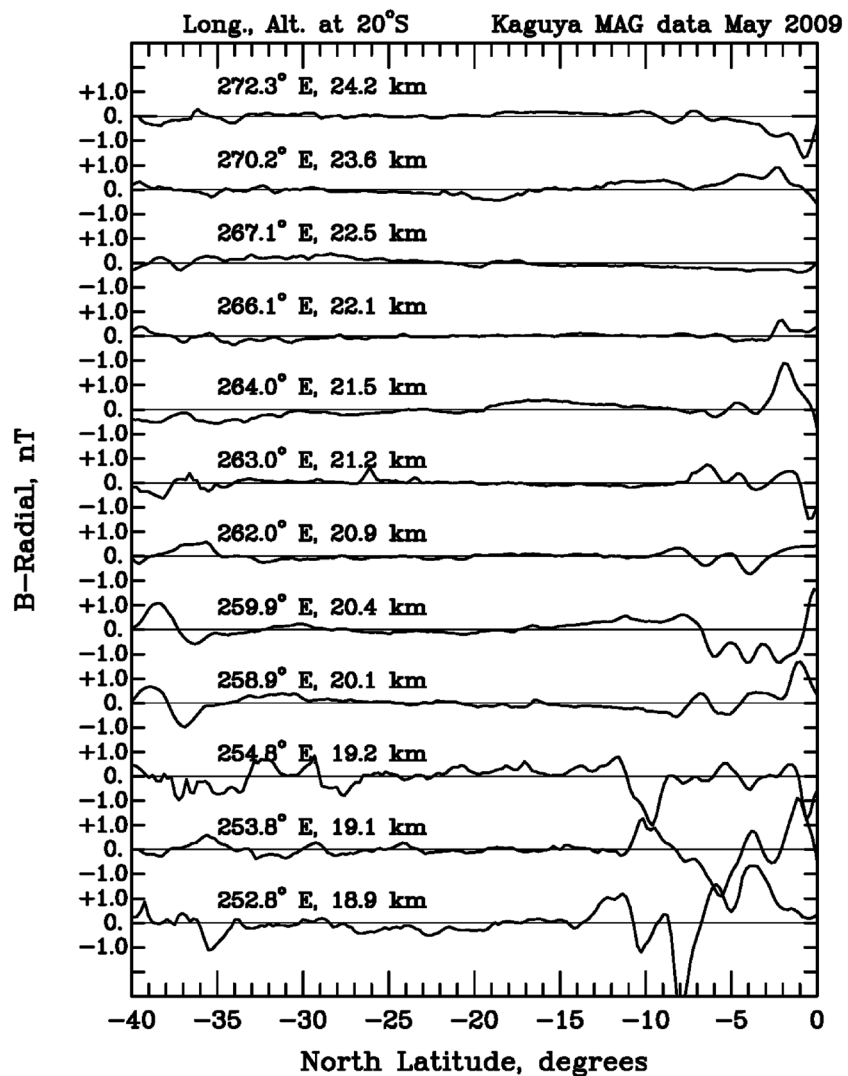


Figure 3. As in Figures 1 and 2 but for a series of 12 Kaguya orbit passes from May 2009 over the Orientale basin. Longitude and altitude at 20°S are indicated at left.

In the case of Orientale, 32 KG passes from 26 to 29 May 2009 covering a region extending from 240°E to 290°E longitude and from 40°S to the equator were selected. The spacecraft altitude ranged from ~17 km on the western side to ~26 km on the eastern side. The Moon was in the solar wind, and the spacecraft was in the lunar wake; however, the spacecraft was near one side of the downstream cavity, so external field variations were significant. Figure 3 plots the radial field component along a subset of 12 of these passes with coverage over the basin center. The increased external field contamination level for these passes as compared to the Imbrium and Schrödinger passes is evident from the lack of repetition of anomaly patterns on successive orbits. The contamination level is even larger for the east and north field components (not shown). No confirmed anomalies can be detected in the central part of the basin (longitudes from ~253°E to 277°E). Further examination of both LP and KG data for all months of both missions did not identify measurements of better quality over this basin.

3. Mapping Methods and Results

Because of the slow lunar rotation rate, adjacent polar orbit passes of a low-altitude spacecraft are typically separated by only about 1° of longitude (~30 km) at the equator. Consecutive passes during a single lunation therefore yield measurements on a slightly curved surface defined by the evolving spacecraft altitude. It is then possible to apply a simple direct mapping method to produce maps of the crustal magnetic field over a

given region on this surface. Alternatively, approximate maps on a constant altitude surface can be produced in which anomaly amplitudes are adjusted for small differences in spacecraft altitude using a power law procedure [e.g., Hood *et al.*, 2013]. However, for measurements obtained at the lowest altitudes (10 to 25 km), the spacecraft altitude can vary substantially (by as much as a factor of 2) across a large impact basin. Also, in some cases, accurate measurements were only obtained for the radial field component, as was described above for LP measurements over Imbrium, for example. A direct mapping method then becomes less than sufficient for producing acceptable maps of the three field components and the field magnitude.

For these reasons, an equivalent source dipole (ESD) mapping technique [Mayhew, 1979; von Frese *et al.*, 1981; Purucker *et al.*, 2000; Langlais *et al.*, 2004; Thébaud *et al.*, 2006] is adopted here for those basins in which anomalies are confirmed to exist. The ESD technique has been applied most recently for mapping of Mercury's crustal field using Mercury Surface, Space ENvironment, GEochemistry, and Ranging (MESSENGER) magnetometer data [Hood, 2015, 2016; Johnson *et al.*, 2016]. This technique allows estimation of the crustal field at a constant altitude using only one measured vector field component and has the advantage that the final mapped field is guaranteed to be a purely potential field. Here a relatively simple "classical ESD" technique [e.g., Purucker *et al.*, 2000] is used in which the sources are assumed to consist of an array of vertically oriented magnetic dipoles at some depth below the planetary surface. The amplitudes and signs of the individual dipole moments are then determined via an iterative least squares fit of the model field to the spacecraft magnetometer measurements along the orbit tracks. Once a final set of dipole moments is determined, these can be applied to estimate the three field components and field magnitude on a constant-altitude surface. The optimal depth of the array for a given spacing of the dipoles is determined by repeating the inversion procedure until a minimum root-mean-square (RMS) deviation of the model radial field values from the observed radial field measurements is obtained. For example, a depth of about 20 km for a dipole array with a horizontal spacing of 1° in latitude and 2° in longitude centered at 55°N latitude was found to be optimal using MESSENGER data [Hood, 2016]. The derived depth of this equivalent source representation does not imply that the true sources are at this depth. For example, distributed sources near the surface could produce nearly the same field at the spacecraft altitude.

To illustrate the application of the ESD technique to lunar data, we consider first the Kaguya orbit passes near Schrödinger, which are relatively complete and free of external fields (see Figure 2 and the description in section 2). Figure 4a plots the 57 low-altitude orbit tracks during 8–12 May 2009 and Figure 4b is a contour map of the spacecraft altitude during these passes, both superposed on color-coded topography based on Clementine laser altimeter data [Smith *et al.*, 1997] (www.mapaplanet.org; orthographic projection). As seen in Figure 4b, the spacecraft altitude ranges from about 19 km to 26 km. This altitude variation alone is not sufficient to require an ESD approach. However, stack plots similar to Figure 2 but for all three vector field components (see Figures S7 and S8) show that the residual east component is significantly affected by external field variations. Hence, use of an ESD technique is a useful improvement.

For this purpose, the sources in the vicinity of Schrödinger were assumed to consist of an array of 41 by 31 radially oriented magnetic dipoles on a spherical surface at some to-be-determined depth beneath the mean lunar radius. The dipoles were spaced 0.5° apart in latitude and 2° apart in longitude covering latitudes from 65°S to 85°S and longitudes from 100°E to 160°E (1200 dipoles). Dipole moment amplitudes were iteratively adjusted positively or negatively depending on the difference between the observed and model field above the location of a given dipole. Convergence to a solution (defined as occurring when the change in RMS deviation between iterations was less than 0.001 nT) occurred after about 50 iterations. By repeating the calculation for a series of assumed depths, it was found that a depth of about 5 km yields a minimum RMS misfit of ~0.4 nT. The final correlation coefficient between the modeled and observed radial field component along the spacecraft orbit tracks within the basin rim was 0.975. For comparison, the corresponding correlation coefficients for the north and east components, which contain more external field contamination, were 0.906 and 0.869, respectively.

Figure 5a plots the radial field component in nT at an altitude of 15 km over Schrödinger calculated from the ESD solution and superposed onto the Clementine topography. To produce an equally spaced array suitable for contour mapping, the model data along the original orbit tracks were first sorted into 1° longitude \times 0.5° latitude bins and were then smoothed two-dimensionally using a 5 \times 5 boxcar filter (i.e., 5° longitude by 2.5° latitude). The chosen altitude is somewhat below the observation altitude of 19–26 km but not so low that significant downward continuation errors are produced. Anomalies within the basin rim are

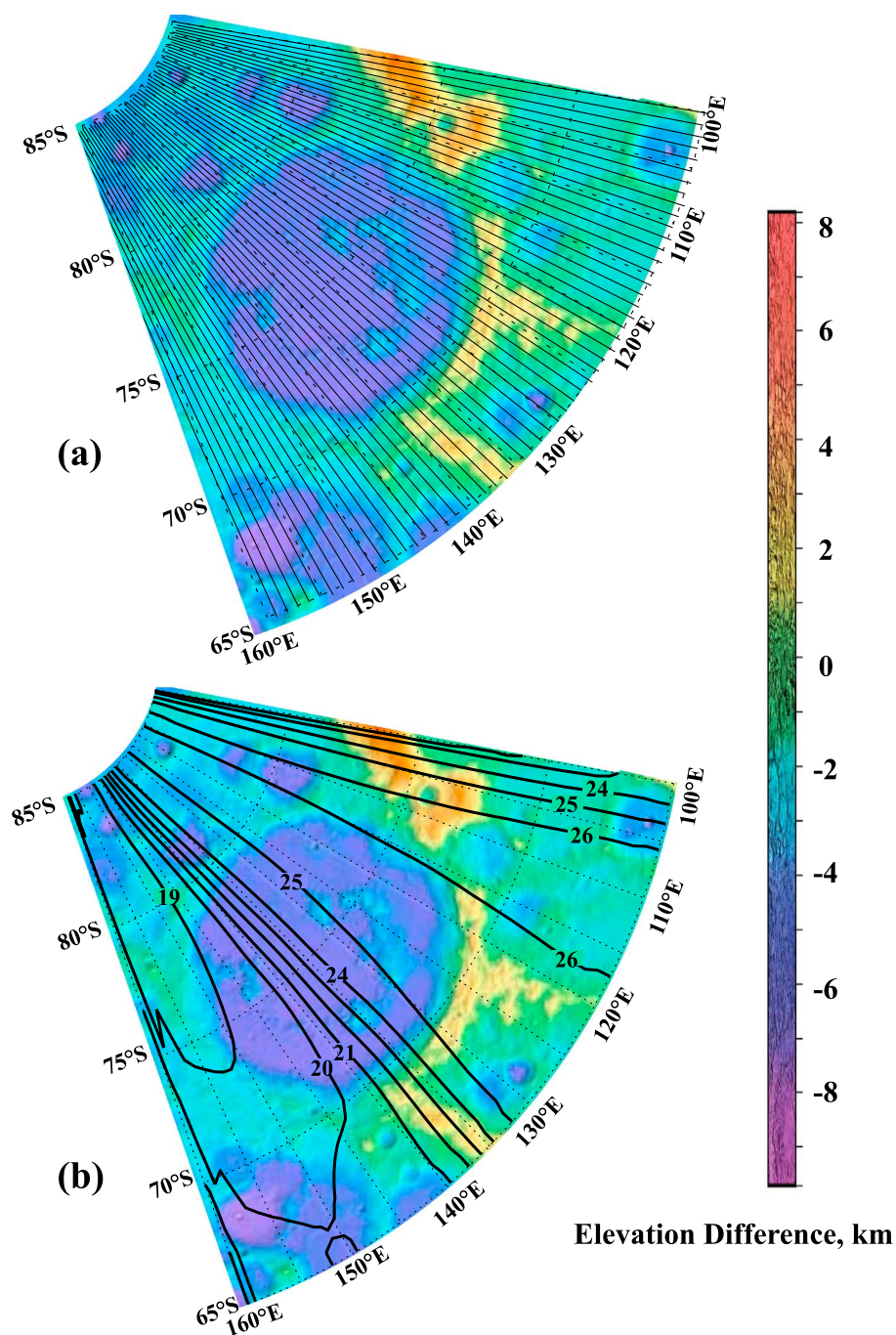


Figure 4. (a) 57 Kaguya orbit tracks from 8 to 12 May 2009 near the Schrödinger basin. (b) Approximate altitude above the mean lunar radius (1737.1 km). Both plots are superposed on Clementine topography (see the text).

seen to be asymmetrically distributed with larger values toward the northwest (lower right) and smaller values toward the southeast (upper left). Figure 5b shows the field magnitude in the same format. These results are not very sensitive to the chosen filter size because the anomalies themselves (Figure 2) have relatively long wavelengths. Smoothing using a 3×3 boxcar filter (3° longitude by 1.5° latitude) yields maps that differ in only minor details from those shown in Figure 5.

Figure 6 shows the field magnitude from Figure 5b superposed onto a Lunar Reconnaissance Orbiter Wide Angle Camera composite image (North is at top). The asymmetrical structure of the internal basin anomalies

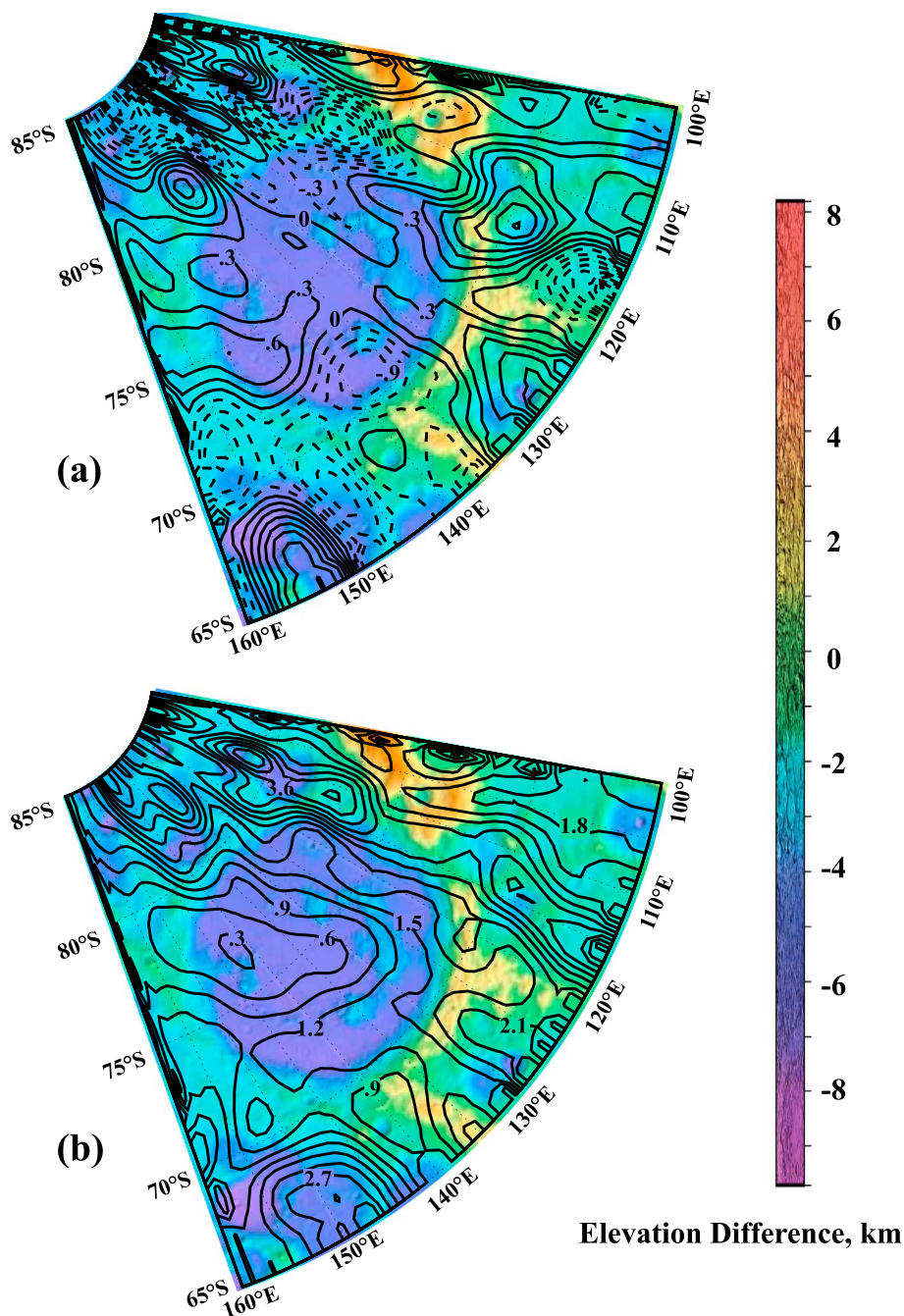


Figure 5. As in Figure 4 but showing (a) the radial magnetic field component and (b) the field magnitude at 15 km altitude within Schrödinger as estimated by the ESD technique. The contour interval is 0.3 nT. The model data have been two-dimensionally smoothed using a 5×5 boxcar filter with a bin size of 1° of longitude by 0.5° of latitude. Superposed on Clementine topography, orthographic projection.

is similar to that of other central basin anomalies on the Moon, e.g., Crisium [Hood, 2011]. This could reflect either an original asymmetry in the distribution of magnetic sources (e.g., impact melt within the basin) or demagnetization effects of later events. It is unlikely that resurfacing by volcanic plains material in the basin alone would have been effective in thermally demagnetizing the anomaly sources because the heat from such a thin molten layer would not penetrate significantly into the interior [e.g., Rumpf et al., 2013]. However, volcanic materials within Schrödinger are concentrated within the basin's semicircular peak ring, and a relatively recent pyroclastic deposit is located to the southeast of the basin center [Mest, 2010]. It is therefore possible

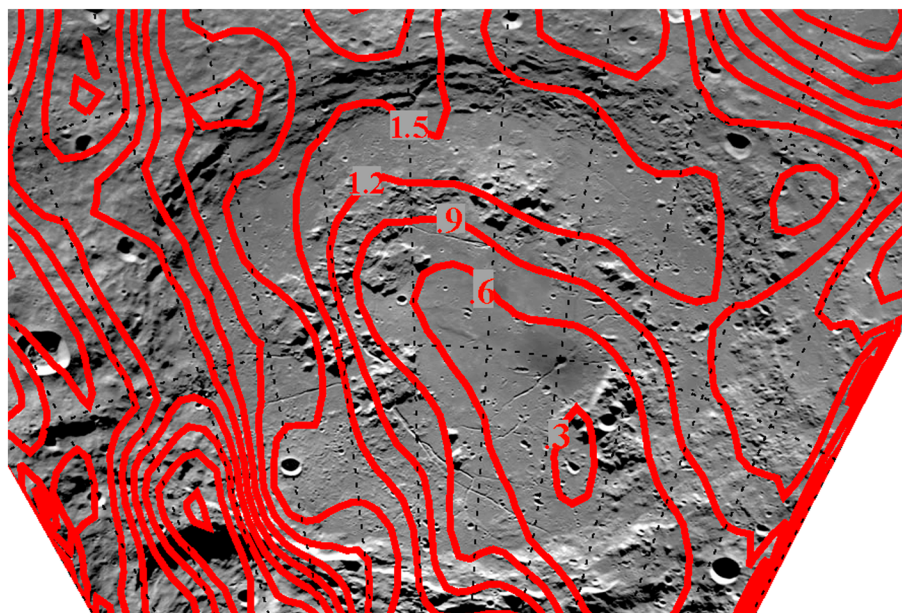


Figure 6. Same field magnitude contour map as in Figure 5b but superposed onto a Lunar Reconnaissance Orbiter Wide Angle Camera composite image (www.lroc.asu.edu). North is at top. A dark deposit caused by a relatively recent pyroclastic eruption from a volcanic cone is visible southeast of the basin center.

that the deeper internal thermal effects of this volcanic activity (e.g., dike swarms) have weakened preexisting subsurface magnetization, leading to the observed asymmetry.

Figure 7 shows results of applying the ESD technique to the radial magnetic field measurements obtained over the Imbrium basin (Figure 1). Figure 7a plots the modeled radial field component, and Figure 7b plots the field magnitude. Figure S5 in the supporting information shows plots for the modeled east and north components. Unlike the KG Schrödinger measurements, which were nearly complete, the edited LP measurements are characterized by missing orbit passes and passes with only partial coverage. To produce a complete map, it was therefore necessary to fill in some missing data with data interpolated from adjacent passes. After doing so, the sources in the vicinity of Imbrium were assumed to consist of an array of 42 by 51 radially oriented magnetic dipoles on a spherical surface beneath the mean lunar radius. The dipoles were spaced 1° apart in both latitude and longitude covering latitudes from 14.5°N to 55.5°N and longitudes from 318°E to 8°E (2142 dipoles). After trial calculations, it was found that a depth of about 40 km produced a minimum RMS misfit (0.156 nT) of the model radial field measurements to the observed measurements along the orbit tracks. Convergence to a solution occurred after about 50 iterations. To produce the contour maps, the model field data at a constant altitude of 15 km along the orbit tracks were first sorted into one third by one third degree bins and were then smoothed two-dimensionally using a 3×3 boxcar filter (i.e., 1.0° longitude by 1.0° latitude). The chosen altitude of 15 km is comparable to the actual altitude of observation, which ranged from 13 to 19 km.

A comparison of the mapped anomalies within the basin rim in Figure 7a with the direct measurements in Figure 1 shows that only the strongest anomaly (smoothed amplitude 1.6 nT near 344°E , 28°N) is repeated on adjacent orbit tracks and is therefore confirmed to be of lunar origin. Weaker anomalies with amplitudes of 0.4 nT or less are not confirmed with the existing data. As emphasized in section 2, the existence of only a single detectable anomaly within Imbrium may be due to external field contamination since anomaly amplitudes less than 1 nT are only marginally detectable. However, their apparent lesser presence in most of the basin suggests that the original magnetization that existed shortly after the basin-forming event may have been modified by demagnetization events later in lunar history. As was the case for Schrödinger, the occurrence of extensive mare volcanism within the basin raises the possibility of thermal demagnetization by volcanic events. While the thin mare basalt layer may not have heated the subsurface to significant depths, it is possible that internal volcanic activity (e.g., feeder dikes) were more effective at heating and demagnetizing the deeper subsurface. The single detected anomaly is centered on a portion of the inner basin ridge ring

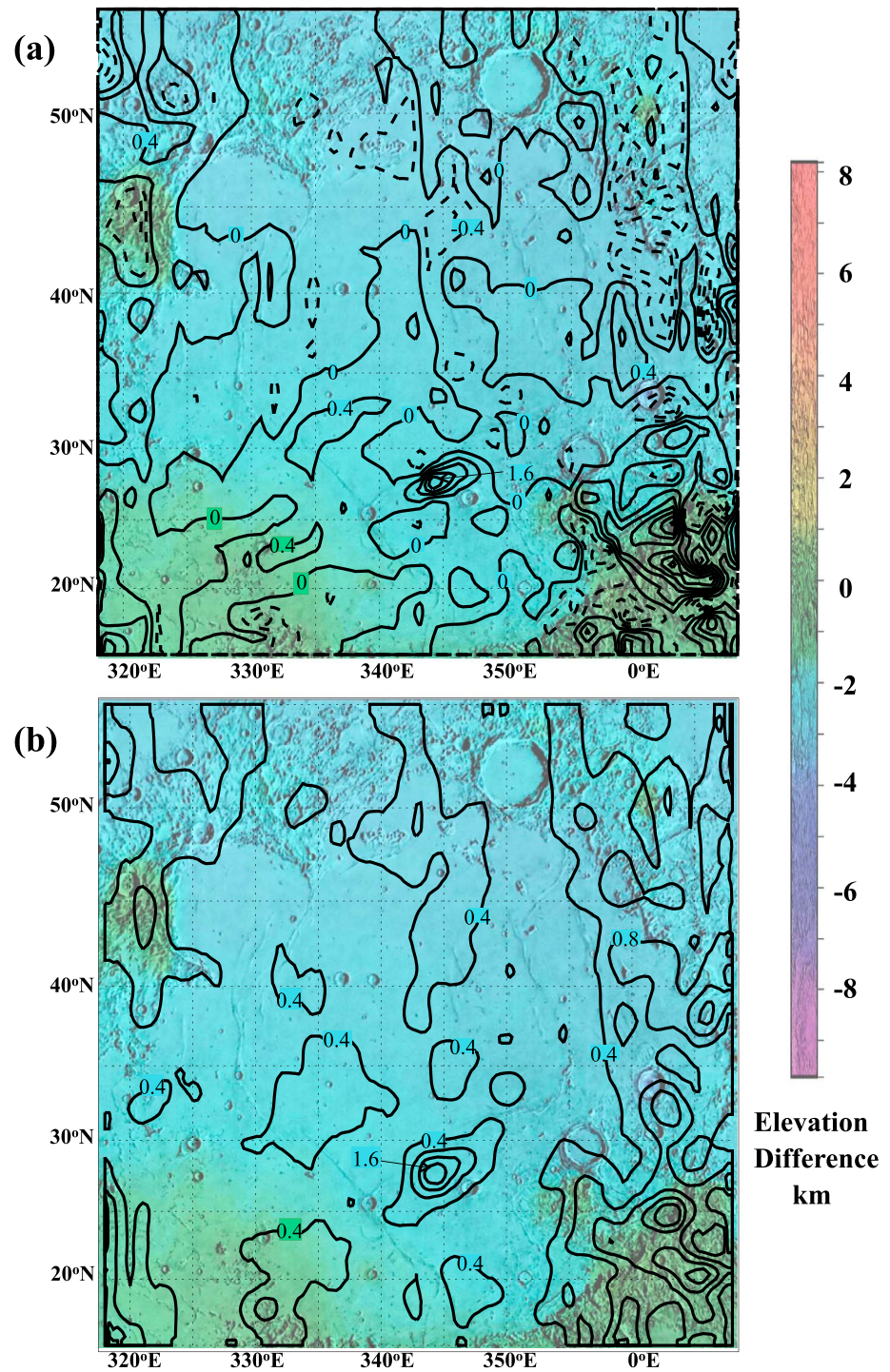


Figure 7. (a) Radial magnetic field component; and (b) the field magnitude at 15 km altitude within the Imbrium basin as estimated by the ESD technique. The contour interval is 0.4 nT. The model data have been two-dimensionally smoothed using a 3×3 boxcar filter with a bin size of 0.33° of longitude by 0.33° of latitude. Superposed on Clementine topography, mercator projection.

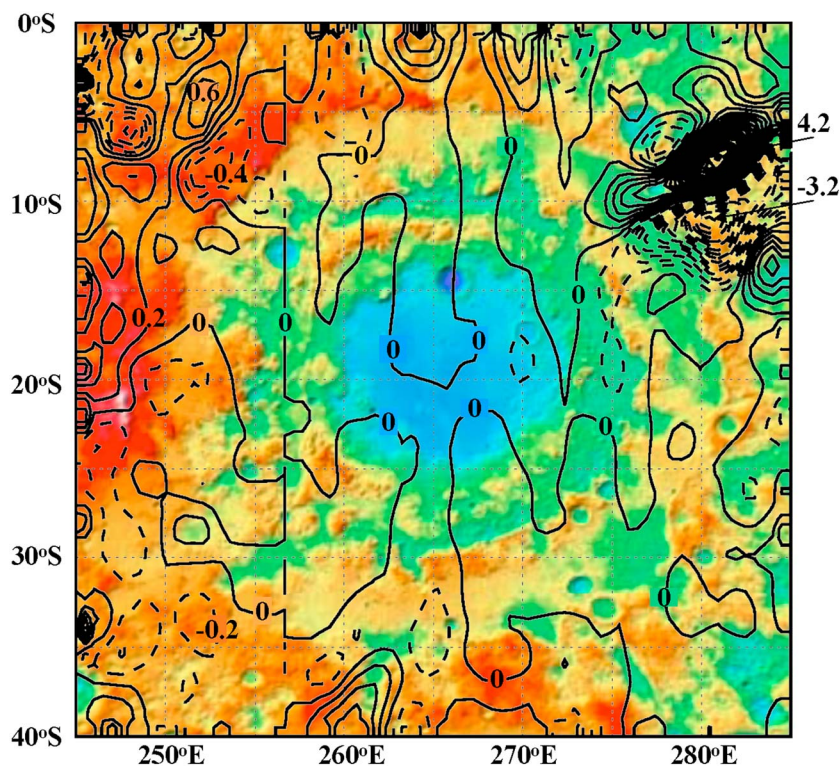


Figure 8. Radial component of the crustal magnetic field at about 25 km altitude in the vicinity of the Orientale Basin superposed on Clementine topography. The contour interval is 0.2 nT. See Figure 7 for the elevation color scale.

(550 km in diameter). The mare basalt layer would be relatively thin here, and it is possible that the original subsurface magnetization was better preserved at this location against volcanic heating effects.

Finally, Figure 8 shows a map of the radial magnetic field component in the vicinity of the Orientale basin at about 25 km altitude produced directly from the orbital measurements of Figure 3. The ESD technique was not applied to these data because of lack of evidence in the individual orbit passes for detectable anomalies. To produce the map, measurements along individual orbit passes were first sorted into $0.5^\circ \times 0.5^\circ$ bins and smoothed using a 5×5 boxcar filter. The spacecraft altitude ranged from about 17 to 26 km, and anomaly amplitudes were adjusted for altitude differences assuming an inverse dependence on altitude. Although no anomalies were detected, it is possible that future measurements at altitudes this low during periods with less external field variability will yield evidence for weak anomalies.

4. Discussion and Conclusions

The anomaly within Imbrium (Figure 7) is not clearly present on recent global maps of the lunar crustal magnetic field produced from LP and KG magnetometer data [Purucker and Nicholas, 2010; Tsunakawa *et al.*, 2015]. It is shown on only one previous ER map [Halekas *et al.*, 2010] and possibly on an early spherical harmonic model map [Purucker *et al.*, 2008]. A likely explanation is that, in the current work, only the best available measurements obtained at the lowest altitudes and with the least amount of external field contamination were identified over a given basin using either the LP or the KG data set. Regional field maps were then constructed considering only the radial field component, which usually has less external field variability than the two horizontal field components.

As noted in section 1, the existence of even weak magnetic anomalies well within a basin rim is very difficult to explain in the absence of a former core dynamo. This is because the post-impact subsurface was heated to very high temperatures, which would have thermally eliminated any preexisting magnetization, and then cooled slowly through the Curie blocking spectrum for metallic iron remanence carriers. Only a steady, long-lived magnetizing field would have imparted coherent magnetization. It is unlikely that the overlying thin mare basalt layer could be the sources of the anomalies because pristine igneous lunar rocks contain almost no

metallic iron remanence carriers [Fuller and Cisowski, 1987; Rochette et al., 2010], and anomalies elsewhere over the lunar maria are weak or nonexistent [e.g., Hood et al., 1979]. Direct magnetometer measurements at the Apollo 15 landing site on the edge of Imbrium in an area dominated by mare basalt yielded only a very weak surface field of ~ 3 nT [Dyal et al., 1974]. There is also no evidence that ejecta from a later basin-forming event (i.e., Orientale) could have been deposited in Imbrium and Schrödinger and that this material could be the sources of the anomalies. The anomalies in Schrödinger are distributed around the basin center, while the detected anomaly in Imbrium is in an isolated part of the basin, neither of which is suggestive of an Orientale ejecta origin. Rather, the most likely explanation is that the sources consist of subsurface material that was heated and melted at the time of impact and subsequently acquired thermoremanent magnetization.

The weakness of anomalies in the Imbrian-aged basins as compared to those found in many Nectarian-aged impact basins has been known for some time [Halekas et al., 2003] and could be due to a number of factors. First, as suggested originally by the latter authors, it is possible that the core dynamo field was significantly less intense during the early Imbrian epoch than during the Nectarian period. Second, it is possible that basin-forming impactors during the Imbrian period were less iron rich than those during the Nectarian period, and this led to a reduced concentration of magnetic carriers in their impact melt rocks. Third, as suggested in section 3, later subsurface volcanic activity may have thermally demagnetized preexisting stronger magnetization during a period when the dynamo was much weaker or absent.

While the third (thermal demagnetization) mechanism could have been significant for Imbrium and Schrödinger, it is less likely to explain the lack of anomalies over Orientale. Geologic maps [Scott et al., 1977] show that, although the central part of the basin contains mare basalt, much of the remaining interior consists of the Maunder Formation, which is interpreted as “probably mostly impact melt.” This exposed solidified impact melt was probably not subjected to later thermal demagnetization and has no detectable magnetic signature. It must therefore either contain very little susceptible material or must have solidified in the presence of a very weak or nonexistent steady magnetizing field. Compositionally, the Maunder Formation is quite feldspathic and low in FeO (~ 4.5 wt %, probably almost all FeO in silicates [e.g., Spudis et al., 2014]), which might support a lesser concentration of metallic iron remanence carriers. However, there is no general tendency for Imbrian-aged basin melt sheets to be depleted in FeO compared to Nectarian-aged basins. In general, the composition of a basin’s melt sheet is mainly dependent on the location of the basin (its crustal target), not the basin age. For example, the Imbrium basin melt is iron rich (8–11 wt % FeO [Spudis and Murl, 2015]), while the Nectaris basin melt is more feldspathic (Fe-poor). Also, a factor of 2 difference in FeO content may not be enough to explain the extreme weakness of anomalies in Imbrian-aged basins compared to those in Nectarian-aged basins.

Acknowledgments

Lunar Prospector calibrated magnetometer data are available from the Planetary Plasma Interactions node of the NASA Planetary Data System (ppi.pds.nasa.gov). Kaguya 4 s averaged magnetometer data are available from the Japan Aerospace Exploration Agency (JAXA) SELENE data archive at <http://l2db.selene.darts.isas.jaxa.jp>. The model data files used to construct the field maps shown in Figures 5, 7, and 8 can be obtained from the following anonymous ftp site: ftp://ftp.lpl.arizona.edu/pub/lpl/ion/moon/jgr_imbrian. The background Clementine elevation maps can be obtained from the U.S. Geological Survey (www.mapaplanet.org). LPI contribution 1985. This work was inspired in part by attendance of a conference on Advances in Lunar Magnetism, organized by M. Wieczorek and B. Weiss, held at Cargèse, Corsica, France, on 1–4 June 2016. The authors thank Jasper Halekas and an anonymous reviewer for very helpful criticisms.

The second (iron-poor impactor) mechanism also is not supported by current views on the origin of planetary impactors in the inner solar system during the late heavy bombardment period when Imbrium, Schrödinger, and Orientale formed. These impactors are believed to have been asteroids that were ejected dynamically from the main asteroid belt, possibly as a consequence of orbital migration of Jupiter and Saturn [e.g., Strom et al., 2005]. Some fraction of these impactors, especially the larger ones, would have contained iron cores. There is therefore no reason to expect a progression of iron-rich impactors producing mainly moderate-sized basins during the Nectarian period to iron-poor impactors producing mainly larger basins during the Imbrian period.

The simplest explanation for the weakness of anomalies in Imbrian-aged basins therefore remains that the magnetizing field strength was much weaker during Imbrian time than it was during earlier epochs, as suggested originally by Halekas et al. [2003]. This conclusion contrasts with sample evidence, which indicates strong paleofields (tens of μT) extending well into the Imbrian period. Without more information to favor an alternate explanation, it must be concluded that, at this point in time, the sample evidence and the orbital evidence do not obviously agree as to the history of lunar magnetism.

References

- Cournède, C., J. Gattacceca, and P. Rochette (2012), Magnetic study of large Apollo samples: Possible evidence for an ancient centered dipolar field on the Moon, *Earth Planet. Sci. Lett.*, *331–332*, 31–42.
- Dyal, P., C. W. Parkin, and W. D. Daily (1974), Magnetism and the interior of the Moon, *Rev. Geophys. Space Phys.*, *12*, 568–591.
- Fischer-Gödde, M., and H. Becker (2011), What is the age of the Nectaris Basin? New Re-Os constraints for a pre-4.0 Ga bombardment history of the Moon, paper presented at 42nd Lunar and Planetary Science Conference, p. 1414, The Woodlands, Tex., 7–11 Mar.
- Fischer-Gödde, M., and H. Becker (2012), Osmium isotope and highly siderophile element constraints on ages and nature of meteoritic components in ancient lunar impact rocks, *Geochim. Cosmochim. Acta*, *77*, 135–156.

- Garrick-Bethell, I., B. P. Weiss, D. L. Shuster, and J. Buz (2009), Early lunar magnetism, *Science*, *323*, 356–359.
- Fuller, M., and S. Cisowski (1987), Lunar paleomagnetism, in *Geomagnetism*, vol. 2, edited by J. Jacobs, pp. 307–456, Academic Press, Orlando, Fla.
- Gattacceca, J., M. Boustie, L. Hood, J.-P. Cuq-Lelandais, M. Fuller, N. Bezaeva, T. de Resseguier, and L. Berthe (2010), Can the lunar crust be magnetized by shock: Experimental groundtruth, *Earth Planet. Sci. Lett.*, *299*, 42–53.
- Halekas, J. S., D. L. Mitchell, R. P. Lin, S. Frey, L. L. Hood, M. H. Acuña, and A. B. Binder (2001), Mapping of crustal magnetic anomalies on the lunar near side by the Lunar Prospector electron reflectometer, *J. Geophys. Res.*, *106*, 27,841–27,852.
- Halekas, J. S., D. L. Mitchell, R. P. Lin, S. Frey, L. Hood, M. Acuña, and A. B. Binder (2002), Demagnetization signatures of lunar impact craters, *Geophys. Res. Lett.*, *29*(13), 1645, doi:10.1029/2001GL013924.
- Halekas, J. S., R. P. Lin, and D. L. Mitchell (2003), Magnetic fields of lunar multi-ring impact basins, *Meteorit. Planet. Sci.*, *38*, 565–578.
- Halekas, J. S., R. J. Lillis, R. P. Lin, M. Manga, M. E. Purucker, and R. A. Carley (2010), How strong are lunar crustal magnetic fields at the surface?: Considerations from a reexamination of the electron reflectometry technique, *J. Geophys. Res.*, *115*, E03006, doi:10.1029/2009JE003516.
- Hood, L. L. (2011), Central magnetic anomalies of Nectarian-aged lunar impact basins: Probable evidence for an early core dynamo, *Icarus*, *211*, 1109–1128.
- Hood, L. L. (2015), Initial mapping of Mercury's crustal magnetic field: Relationship to the Caloris impact basin, *Geophys. Res. Lett.*, *42*, 10,565–10,572, doi:10.1002/2015GL066451.
- Hood, L. L. (2016), Magnetic anomalies concentrated near and within Mercury's impact basins: Early mapping and interpretation, *J. Geophys. Res. Planets*, *121*, 1016–1025, doi:10.1002/2016JE005048.
- Hood, L. L., P. J. Coleman, C. T. Russell Jr., and D. E. Wilhelms (1979), Lunar magnetic anomalies detected by the Apollo subsatellite magnetometers, *Phys. Earth Planet. Inter.*, *20*, 291–311.
- Hood, L. L., A. Zakharian, J. Halekas, D. Mitchell, R. Lin, M. Acuña, and A. Binder (2001), Initial mapping and interpretation of lunar crustal magnetic anomalies using Lunar Prospector magnetometer data, *J. Geophys. Res.*, *106*, 27,825–27,839.
- Hood, L. L., N. C. Richmond, and P. D. Spudis (2013), Origin of strong lunar magnetic anomalies: Further mapping and examinations of LROC imagery in regions antipodal to young large impact basins, *J. Geophys. Res. Planets*, *118*, 1265–1284, doi:10.1002/jgre.20078.
- Hood, L. L., H. Tsunakawa, and P. D. Spudis (2014), Central magnetic anomalies in old lunar impact basins: New constraints on the earliest history of the former core dynamo, paper presented at 45th Lunar and Planetary Science Conference, p. 1482, The Woodlands, Tex., 17–21 Mar.
- Ivanov, B. A. (2005), Numerical modeling of the largest terrestrial meteorite craters, *Sol. Syst. Res.*, *39*, 381–409.
- Johnson, C. L., et al. (2016), Mercury's lithospheric magnetic field, paper presented at 47th Lunar and Planetary Science Conference, p. 1391, The Woodlands, Tex., 21–25 Mar.
- Langlais, B., M. E. Purucker, and M. Manda (2004), Crustal magnetic field of Mars, *J. Geophys. Res.*, *109*, E02008, doi:10.1029/2003JE002048.
- Lin, R. P., D. Mitchell, D. Curtis, K. Anderson, C. Carlson, J. McFadden, M. Acuña, L. Hood, and A. Binder (1998), Lunar surface magnetic fields and their interaction with the solar wind: Results from Lunar Prospector, *Science*, *281*, 1480–1484.
- Mayhew, M. A. (1979), Inversion of satellite magnetic anomaly data, *J. Geophys.*, *45*, 119–128.
- Merle, R. E., A. A. Nemchin, M. L. Grange, M. J. Whitehouse, and R. T. Pidgeon (2014), High resolution U-Pb ages of Ca-phosphates in Apollo 14 breccias: Implications for the age of the Imbrium impact, *Meteorit. Planet. Sci.*, *49*, 2241–2251.
- Mest, S. C. (2010), The geology of Schrödinger basin: Insights from post-Lunar Orbiter data, *Geol. Soc. Am. Spec. Pap.*, *477*, 95–115, doi:10.1130/2011.2477(04).
- Mitchell, D. L., J. S. Halekas, R. P. Lin, S. Frey, L. L. Hood, M. H. Acuña, and A. Binder (2008), Global mapping of lunar crustal magnetic fields by Lunar Prospector, *Icarus*, *194*, 401–409.
- Purucker, M. E., and J. B. Nicholas (2010), Global spherical harmonic models of the internal magnetic field of the Moon based on sequential and coestimation approaches, *J. Geophys. Res.*, *115*, E12007, doi:10.1029/2010JE003650.
- Purucker, M., D. Ravat, H. Frey, C. Voorhies, T. Sabaka, and M. Acuña (2000), An altitude-normalized magnetic map of Mars and its interpretation, *Geophys. Res. Lett.*, *27*, 2449–2452.
- Purucker, M. E., J. W. Head, and J. S. Halekas (2008), Magnetic signatures of lunar multi-ringed impact basins: New constraints on the timing of the putative lunar dynamo, paper presented at 39th Lunar and Planetary Science Conference, p. 1655, League City, Tex., 10–14 Mar.
- Rochette, P., J. Gattacceca, A. V. Ivanov, M. A. Nazarov, and N. S. Bezaeva (2010), Magnetic properties of lunar materials: Meteorites, Luna and Apollo returned samples, *Earth Planet. Sci. Lett.*, *292*, 383–391.
- Rumpf, M. E., S. A. Fagents, I. A. Crawford, and K. H. Joy (2013), Numerical modeling of lava-regolith heat transfer on the Moon and implications for the preservation of implanted volatiles, *J. Geophys. Res. Planets*, *118*, 382–397, doi:10.1029/2012JE004131.
- Ryder, G. (2002), Mass flux in the ancient Earth-Moon system and benign implications for the origin of life on Earth, *J. Geophys. Res.*, *107*(E4), 5022, doi:10.1029/2001JE001583.
- Shea, E. K., B. P. Weiss, W. S. Cassata, D. L. Shuster, S. M. Tikoo, J. Gattacceca, T. L. Grove, and M. D. Fuller (2012), A long-lived lunar core dynamo, *Science*, *335*, 453–456.
- Scott, D. H., J. F. McCauley, and M. N. West (1977), *Geologic Map of the West Side of the Moon*, U.S. Geol. Surv. Map I-1034, Arlington, Va.
- Smith, D. E., M. T. Zuber, G. A. Neumann, and F. G. Lemoine (1997), Topography of the Moon from the Clementine lidar, *J. Geophys. Res.*, *102*, 1591–1611.
- Spudis, P. D., and J. N. Murl (2015), Impact melt from lunar multi-ring basins: Orientale and Imbrium, paper presented at 46th Lunar and Planetary Science Conference, p. 1853, The Woodlands, Tex., 16–20 Mar.
- Spudis, P. D., D. J. P. Martin, and G. Kramer (2014), Geology and composition of the Orientale Basin impact melt sheet, *J. Geophys. Res. Planets*, *119*, 19–29, doi:10.1002/2013JE004521.
- Strangway, D. W., H. Sharpe, W. Gose, and G. Pearce (1973), Lunar magnetic anomalies and the Cayley Formation, *Nature*, *246*, 112–114.
- Strom, R. G., R. Malhotra, T. Ito, F. Yoshida, and D. A. Kring (2005), The origin of planetary impactors in the inner solar system, *Science*, *309*, 1847–1850.
- Suavet, C., B. P. Weiss, W. Cassata, D. Shuster, J. Gattacceca, L. Chan, I. Garrick-Bethell, J. W. Head, T. Grove, and M. D. Fuller (2013), Persistence and origin of the lunar core dynamo, *Proc. Natl. Acad. Sci. U.S.A.*, *110*, 8453–8458.
- Thébault, E., J. J. Schott, and M. Manda (2006), Revised spherical cap harmonic analysis (R-SCHA): Validation and properties, *J. Geophys. Res.*, *111*, B01102, doi:10.1029/2005JB003836.
- Tikoo, S. M., B. P. Weiss, W. S. Cassata, D. L. Shuster, J. Gattacceca, E. A. Lima, C. Suavet, F. Nimmo, and M. D. Fuller (2014), Decline of the lunar core dynamo, *Earth Planet. Sci. Lett.*, *404*, 89–97.

- Tsunakawa, H., H. Shibuya, F. Takahashi, H. Shimizu, M. Matsushima, A. Matsuoka, S. Nakazawa, H. Otake, and Y. Iijima (2010), Lunar magnetic field observation and initial global mapping of lunar magnetic anomalies by MAP-LMAG onboard SELENE (Kaguya), *Space Sci. Rev.*, *154*, 219–251.
- Tsunakawa, H., F. Takahashi, H. Shimizu, H. Shibuya, and M. Matsushima (2015), Surface vector mapping of magnetic anomalies over the Moon using Kaguya and Lunar Prospector observations, *J. Geophys. Res. Planets*, *120*, 1160–1185, doi:10.1002/2014JE004785.
- von Frese, R. R. B., W. J. Hinze, and L. W. Braille (1981), Spherical Earth gravity and magnetic anomaly analysis by equivalent point source inversion, *Earth Planet. Sci. Lett.*, *53*, 69–83.
- Wang, H., and B. P. Weiss (2016), Lifetime of the lunar dynamo constrained by the young Apollo regolith breccia 15015, Abstract GP13A-06 presented at 2016 Fall Meeting, AGU, San Francisco, Calif., 12–16 Dec.
- Weiss, B. P., and S. M. Tikoo (2014), The lunar dynamo, *Science*, *346*, 1198–1208.
- Wieczorek, M. A., and B. P. Weiss (2010), Testing the lunar dynamo hypothesis using global magnetic field data, paper presented at 41st Lunar and Planetary Science Conference, p. 1625, The Woodlands, Tex., 1–5 Mar.
- Wilhelms, D. E. (1987), The geologic history of the Moon, *U.S. Geol. Surv. Prof. Pap.*, *1348*, 302.